ELSEVIER

Catalysis Today 28 (1996) 275–295

CATALYSIS TODAY

The effect of the phase composition of model VPO catalysts for partial oxidation of *n*-butane

V.V. Guliants [a,1], J.B. Benziger [a,*], S. Sundaresan [a], I.E. Wachs [b], J.-M. Jehng [b], J.E. Roberts [b]

[a] *Princeton Materials Institute, Princeton University, Princeton, NJ 08544, USA*
[b] *Zettlemoyer Center for Surface Studies, Lehigh University, Bethlehem, PA 18015, USA*

Abstract

X-ray diffraction, Raman spectroscopy, ^{31}P MAS-NMR and spin-echo NMR indicated that model vanadium phosphorus oxide (VPO) precursors and catalysts contained various minor phases depending on both the synthetic approach and P/V ratios used. Raman spectroscopy revealed the presence of a number of micro-crystalline and amorphous V(IV) and V(V) phases not evident by XRD. The presence of $VOPO_4$ phases was detrimental to the performance of the VPO catalysts for *n*-butane oxidation. The best model organic VPO catalyst contained only vanadyl pyrophosphate with the highest degree of stacking order and virtually no $VOPO_4$ phase impurity. Raman spectroscopy detected vanadyl metaphosphate, $VO(PO_3)_2$, in the catalysts derived from aqueous precursors possessing P/V ratios greater than 1. Pure vanadyl metaphosphate catalyst was inactive in *n*-butane oxidation. ^{31}P NMR demonstrated the absence of vanadyl metaphosphate and other impurity phases in the best catalyst derived from organic precursors at P/V = 1.18. The experimental data strongly indicate that the best VPO catalysts for *n*-butane oxidation contain only vanadyl pyrophosphate with well-ordered stacking of the (200) planes.

Keywords: Phase composition; Model VPO catalysts; Partial oxidation of *n*-butane

1. Introduction

The vanadium–phosphorus–oxide (VPO) system is a commercial catalyst for the 14-e$^-$ selective oxidation of *n*-butane to maleic anhydride. Several V(IV) and V(V) phosphate phases exist in the VPO system and the correlation of catalytic performance with crystalline structure has been reviewed [1–5]. Vanadyl pyrophosphate has been identified as critical for active and selective industrial catalysts [4]. Vanadyl pyrophosphate is obtained from vanadyl(IV) hydrogen phosphate hemihydrate, $VOHPO_4 \cdot 0.5H_2O$, by dehydration.

The synthesis route to achieve the optimal vanadyl pyrophosphate catalyst, and the specific surface of the catalyst remain largely open questions. A common hypothesis is that vanadyl pyrophosphate is a support for some other VPO phase which is active in hydrocarbon oxidation. Some argue that the V^{5+}/V^{4+} dimeric species in the topmost oxidized layer of vanadyl pyro-

* Corresponding author. Department of Chemical Engineering, Princeton University, Princeton, NJ 08544, USA. Phone: 609-258-5416. FAX: 609-258-0211. E-mail: benziger@princeton.edu.

[1] Present address: Praxair, Inc., 175 East Park Drive, P.O. Box 44, Tonawanda, NY 14151-0044, USA.

PII S0920-5861(96)00043-0

phosphate are the active sites [6], while others believe that the active sites lie within the microdomains of crystalline vanadyl(V) orthophosphates, β, α_{II}, δ and γ-$VOPO_4$, formed on the (200) faces of vanadyl pyrophosphate under the catalytic reaction conditions [1,7]. Recently, vanadyl(IV) dihydrogen phosphate, $VO(H_2PO_4)_2$, was suggested as a thermal precursor of an amorphous component of the VPO catalysts which is active in partial oxidation of *n*-butane to maleic anhydride [8].

Both the phase composition and catalytic activity of VPO catalysts depend on the synthesis route for the precursors to the final catalyst. The evolution of the catalyst from its precursors has been followed by XRD, Raman spectroscopy and ^{31}P NMR spectroscopy to elucidate the key synthesis procedures for reference VPO phases and VPO catalysts prepared by aqueous and organic synthesis routes [8–11]. The application of Raman spectroscopy and ^{31}P spin-echo NMR provided greater sensitivity to the phase composition of the VPO catalysts than available from traditional XRD analysis. Specifically, the fingerprint quality of Raman spectroscopy in the low frequency range shows greater sensitivity to the short-range order in metal oxides than infrared spectroscopy [12,15], and has already proven to be instrumental in establishing more accurate phase compositions in VPO system [7,13,14]. Spin-echo NMR [16] decouples $3d^1$ V(IV) ions from the ^{31}P spin which has afforded ^{31}P NMR spectra with excellent resolution permitting the identification of different V(IV) phases in the VPO catalysts.

Spectroscopic analyses presented here identified the existence of micro-crystalline or amorphous phases in VPO precursors and catalysts prepared by different synthetic approaches. These impurity phases affect performance in *n*-butane oxidation. The use of multiple analytical techniques greatly improves our ability to predict catalyst performance; however the structure of the catalyst surface remains unresolved as the techniques applied have limited sensitivity to amorphous and surface phases.

2. Experimental

2.1. Synthesis

2.1.1. Reference compounds

The following reference VPO phases were synthesized according to reported procedures: $VOHPO_4 \cdot 0.5H_2O$ [1], $(VO)_2P_2O_7$ [1], α_I-$VOPO_4$ [17], and γ-$VOPO_4$ [1], $VO(H_2PO_4)_2$ [18], $VO(PO_3)_2$ [18], $V(PO_3)_3$ [19], $VOHPO_4 \cdot H_2O$ [2], α-$VOHPO_4 \cdot 2H_2O$ [2], β-$VOHPO_4 \cdot 2H_2O$ [2] and $VOHPO_4 \cdot 4H_2O$ [2]. X-ray diffraction and thermal gravimetric analysis of these reference compounds agreed well with those reported in the literature. Reference $V(PO_3)_3$ was synthesized similar to a reported procedure [19]: V_2O_5 and the 20-fold excess of $(NH_4)_2HPO_4$ were comminuted, and the mixture heated at 773 K in air for 3 h to decompose $(NH_4)_2HPO_4$. The mixture was then heated at 1073 K in air for another 48 h, after which light green crystals were obtained. Powder XRD confirmed these crystals to be $V(PO_3)_3$ [20].

2.1.2. Aqueous catalysts

VPO catalyst precursors were prepared following the aqueous medium synthesis procedures proposed by Yamazoe and co-workers [8]. The basic procedure is outlined in Fig. 1. Vana-

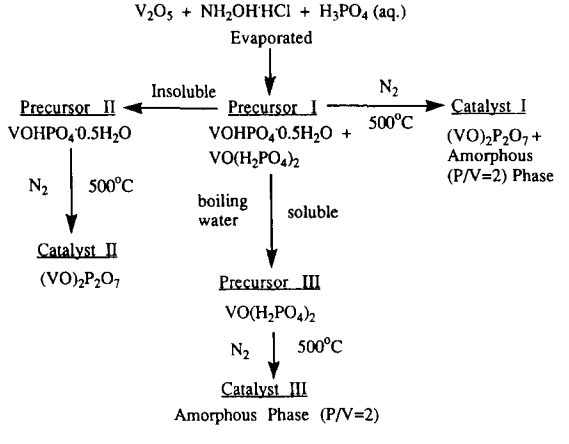

Fig. 1. Preparation of the aqueous precursors, A:P:(I–III):1 and A:P:(I–III):1.7, and corresponding catalysts, A:C:(I–III):1 and A:C:(I–III):1.7 according to [8].

dium pentoxide is reduced in an aqueous solution of $NH_2OH \cdot HCl$ and H_3PO_4 at 353 K, the solvent is evaporated, and the product dried at 393 K, producing vanadyl hydrogen phosphate hemihydrate, $VOHPO_4 \cdot 0.5H_2O$ and vanadyl dihydrogen phosphate, $VO(H_2PO_4)_2$, or vanadyl hydrogen phosphate dihydrate, α-$VOHPO_4 \cdot 2H_2O$. The hemihydrate is water insoluble and can be recovered in more pure form by dissolving the dihydrogen phosphate and dihydrate in boiling water. This procedure is used to produce aqueous precursors I, II and III, where I is the initial solid, II is the purified hemihydrate recovered, and III is the water soluble VPO fraction. All three precursors were dried in air at 393 K. This procedure has been followed with P/V ratios of 1.0 and 1.7. The corresponding catalytic phases were prepared by heating to 773 K in N_2 for 2 h. The P/V ratio is set by the molar amounts of H_3PO_4 and V_2O_5 used in the synthesis. We will designate these materials by the set of terms A:P(or C):I:1.7 for aqueous synthesis route: precursor(or catalyst): Fraction I: P/V ratio of 1.7.

2.1.3. Organic catalysts

Organic catalysts possessing synthetic P/V ratios of 1.18 and 1.5 were synthesized according to an existing patent procedure [9]. V_2O_5 (10 g) was reduced by refluxing, in a mixture of 100 ml of isobutanol and 10 ml of benzyl alcohol for 14 h. Anhydrous orthophosphoric acid dissolved in isobutanol was added slowly over a 2 h period to achieve the desired synthetic P/V ratios and the reflux continued for another 20 h. The resulting blue slurry was filtered, washed with small quantities of isobutanol and acetone, and then dried in air at 383 K for 2 days. The hemihydrate precursors obtained (designated O:P:I:1.18 or O:P:I:1.5) were calcined in flowing nitrogen for 2 h at 823 K to yield grey solids found by XRD and Raman to be pure vanadyl pyrophosphate, denoted as O:C:I:1.18 and O:C:I:1.5, respectively. The latter solids were converted to V(V) orthophosphates (O:C:III:1.18 and O:C:III:1.5) by calcining them in flowing oxygen at 1073 K for 9 h. These VPO species all had a rosette morphology.

2.1.4. Model organic catalysts

Synthesis of model VPO catalysts with platelet morphology to expose specific crystallographic planes is described in detail elsewhere [15,21]; the procedure is outlined in Fig. 2. $VOPO_4 \cdot 2H_2O$ was prepared by reacting V_2O_5 with a 7-fold excess of aqueous H_3PO_4 according to Ladwig [22]. The hemihydrate precursors M:P:I:A (57 mol% yield) and M:P:I:B (90 mol% yield) were obtained by reducing $VOPO_4 \cdot 2H_2O$ in refluxing 2-butanol for 2 and 24 h, respectively. Molar yields were determined as the ratio of the moles of $VOHPO_4 \cdot 0.5H_2O$ precursors obtained to the moles of $VOHPO_4 \cdot 0.5H_2O$ expected from reduction of $VOPO_4 \cdot 2H_2O$. The vanadium hydrogen phosphate hemihydrate precursors were calcined at 823 K in flowing nitrogen for 2 h, M:C:I:A (or B); then, oxidized in flowing oxygen at 773 K for 2 h, M:C:II:A (or B). The oxidized catalysts were suspended in water, stirred for 3 h, filtered, washed with large

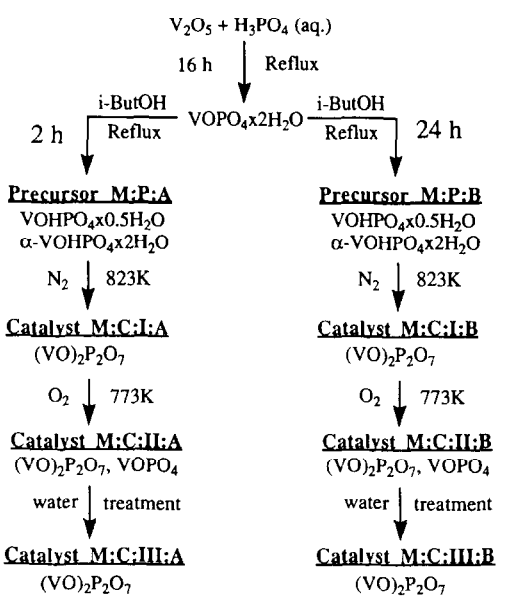

Fig. 2. Preparation of the model organic precursors, M:P:A and M:P:B, and corresponding catalysts, M:C:(I–III):A and M:C:(I–III):B, according to [15].

excess of water and dried in air at room temperature [15] to remove the water soluble phosphate phases. The resulting grey solids were denoted as catalysts M:C:III:A or B, respectively.

2.2. Characterization

Powder X-ray diffraction patterns were recorded with Scintag/USA DMS 2000 diffractometer using a Cu K_α radiation.

The Raman spectra were obtained with a Spectra-Physics Ar^+ laser (model 171) by using ca. 25–50 mW of the 514.5 nm line for excitation. About 100–200 mg of the powdered solid was pressed into a thin wafer about 1 mm thick with KBr backing for support. The sample was then mounted onto a spinning sample holder and rotated at ca. 2000 rpm to avoid local heating effects. A 90° collection geometry was employed to collect the scattered light. Raman spectra were obtained with a Spex Triplemate spectrometer (model 1877) coupled to an EG and G OMA III optical multichannel analyzer (model 1463).

BET surface areas were measured by nitrogen adsorption on Quantachrome Quantasorb system.

The ^{31}P NMR experiments were performed at a resonance frequency near 121.5 MHz in a GN-300 NMR spectrometer equipped with DOTY Scientific, Inc., 7 mm double air bearing MAS probe (0.35 cm^3 sample volume). A radiofrequency (RF) feedback control circuit [23] kept RF field strengths constant. Proton decoupling (300.1 MHz) at 50 kHz RF field strength was used for all spectra. An experimental technique similar to the one previously described [16] was used in this study. Since paramagnetic V(IV) and V(III) materials produce very broad NMR features, the spin-echo method under static conditions was employed to obtain the free induction decay (FID) signal. The Hahn echo pulse sequence was 90°_x–τ–180°_y–acquire with appropriate phase cycling to cancel out artifacts [24]. The 90° pulse was 4.5 μs and τ was 20 μs. The dwell, acquisition and relaxation delay times were 1 μs, 2.05 ms, and 100 ms, respectively. The Fourier transform of the FID from the center of the echo to time infinity provided the frequency domain signal at the carrier frequency. FIDs were multiplied by an exponential function equivalent to 500 Hz before Fourier transformation. In this study, the spectral range from −1000 to 5000 ppm referenced to the resonance frequency of ^{31}P in 85% H_3PO_4 was divided into three equal intervals. The spin-echo spectra were collected varying the carrier frequency in increments of 50 ppm within each spectral interval. The probe was tuned at the center frequency of each new interval before collecting the 40 spectra for that interval. Typically, the number of acquisitions was in the 125–512 range. The reported spectra are obtained by plotting the background corrected intensity of the signal at each incremental carrier frequency. In the case of diamagnetic V(V) orthophosphates, ^{31}P NMR spectra were obtained under MAS conditions at 4 kHz using a single 4.5 μs pulse and a recycle delay of 15 s to produce quantitative spectra.

2.3. Kinetic tests

Oxidation of *n*-butane was carried out with ca. 1 g of catalyst placed into a U-tube Pyrex glass reactor inside an aluminum split block. The reactor was heated in the 1.2% *n*-butane flow to 723 K, after which the reaction products were collected and analyzed for up to 150 h under the catalytic reaction conditions. Product yields evolved over time and were nearly stable after 100 h. Conversion and product selectivity data were all collected after the catalyst stabilized (as determined by $< 0.5\%$ change in conversion and selectivity over a 12 h period). All experiments were carried out in a once-through integral mode. The Weisz–Prater parameter was estimated to be < 0.1 under the reaction conditions employed in these studies indicating diffusional limitations could be neglected [25]. CP grade *n*-butane from Matheson and dry house

air were metered separately using Brooks model 52-36A1V series mass flow controllers with model 5876 two-channel power supply box and mixed in desired proportions. Only a small fraction of the total flow was metered to the reactor with the rest being vented.

The effluent stream was analyzed by on-line gas chromatography. A side stream ran from the heated effluent line to a HP 5790A series gas chromatograph where partial oxidation products (mainly MA and traces of acetic and acrylic acids) were separated on a 2 m long Porapak QS column. After the partial oxidation products were stripped from the effluent by passing through a water bubbler, the effluent samples from a sample loop were injected into two GC columns in series: a 5 m long 30% bis-2-ethoxyethyl sebacate column to separate CO_2 and butane, and a 4 m long 13X molecular sieves column to separate O_2, N_2, and CO. The lines running from the reactor to the HP 5790A gas chromatograph and the water bubbler were kept at 420 K to prevent condensation of maleic anhydride. The GC analysis for maleic anhydride was checked by periodic acid–base titrations of the bubbler solution using a phenolphthalein indicator. The bubbler solution was sampled after passing the effluent through the deionized water in the bubbler at a constant space velocity for 1 h. Concentrations of carbon oxides, butane, nitrogen and oxygen in the effluent were determined using the calibration gas mixture (Airco) containing certified concentrations of the above gases. Closure on the overall carbon balances was $\pm 5\%$.

3. Results

3.1. Raman spectra of reference VPO phases

To exploit the fingerprinting capabilities of Raman spectroscopy reference vanadyl phosphates were synthesized and characterized by XRD, TGA and Raman spectroscopy; the Raman spectra of the reference phases are shown

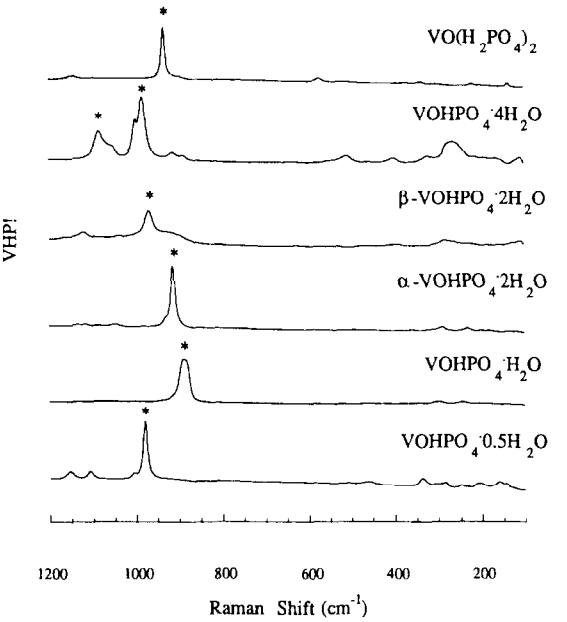

Fig. 3. Raman spectra of reference precursor VPO phases: $VOHPO_4 \cdot 0.5H_2O$, $VOHPO_4 \cdot H_2O$, α-$VOHPO_4 \cdot 2H_2O$, β-$VOHPO_4 \cdot 2H_2O$, $VOHPO_4 \cdot 4H_2O$ and $VO(H_2PO_4)_2$: * characteristic Raman bands.

in Figs. 3 and 4; the Raman and XRD peaks used for compound identification are tabulated in Table 1. The major Raman peaks in the spectra of $VOHPO_4 \cdot 0.5H_2O$, $(VO)_2P_2O_7$ and the V(V) orthophosphates agree with those reported in the literature [14]; but our samples produced better spectra which permitted identification of weaker features not previously reported. The Raman spectra of $VOHPO_4 \cdot H_2O$, α-$VOHPO_4 \cdot 2H_2O$, β-$VOHPO_4 \cdot 2H_2O$, $VOHPO_4 \cdot 4H_2O$, $VO(H_2PO_4)_2$, $VO(PO_3)_2$ and $V(PO_3)_3$ have not been previously reported. For identification of minor phases we used the strongest Raman bands, which are in italic in Table 1 and highlighted in Figs. 3 and 4. These correspond to the asymmetric P–O stretch in the PO_4 groups circa 900–1000 cm^{-1}, the V–O stretch in the vanadyl octahedra circa 1000 cm^{-1}, and the V–O–P stretch circa 1000–1100 cm^{-1}. The pyrophosphates can be distinguished from the orthophosphates and hydrogen phosphates by the presence of a P–O–P symmetric stretch feature circa 800 cm^{-1}, which comes

Table 1
The XRD and Raman peaks of some reference VPO phases at room temperature [a]

$VOHPO_4 \cdot 0.5H_2O$	
XRD peaks 2Θ, *d* (intensity)	15.57°, 5.69 Å (100); 19.67°, 4.51 Å (32); 24.27°, 3.67 Å (24); 27.12°, 3.29 Å (29); 28.75°, 3.11 Å (14); 30.46°, 2.94 Å (51); 32.07°, 2.79 Å (12); 33.71°, 2.66 Å (15); 47.85, 1.90 Å (9)
Raman peaks (cm^{-1})	1154 M, 1109 M, 1007 W, *981 vS*, 509 vW, 461 W, 339 M, 285 W, 250 vW, 232 vW, 210 W, 203 W, 161 W, 146 W
$VOHPO_4 \cdot H_2O$	
XRD peaks 2Θ, *d* (intensity)	13.67°, 6.47 Å (45); 15.73°, 5.63 Å (32); 18.37°, 4.83 Å (23); 20.05°, 4.43 Å (26); 28.26°, 3.16 Å (100)
Raman peaks (cm^{-1})	1002 W, 983 W, *888 vS*, 342 W, 297 M br, 244 M br
α-$VOHPO_4 \cdot 2H_2O$	
XRD peaks 2Θ, *d* (intensity)	11.73°, 7.54 Å (75); 15.21°, 5.82 Å (13); 16.74°, 5.29 Å (19); 21.26°, 4.18 Å (11); 26.11°, 3.41 Å (19); 28.77°, 3.10 Å (100); 31.65°, 2.82 Å (11); 32.14°, 2.78 Å (10); 38.77°, 2.32 Å (13)
Raman peaks (cm^{-1})	1135 W, 1117 W, 1048 M br, 930 sh, *913 vS*, 360 W, 320 W, 289 M, 231 M, 199 W
β-$VOHPO_4 \cdot 2H_2O$	
XRD peaks 2Θ	13.72°, 6.45 Å (19); 15.92°, 5.56 Å (100); 19.35°, 4.58 Å (58); 20.35°, 4.36 Å (59); 23.27°, 3.82 Å (44); 28.14°, 3.17 Å (27); 28.73°, 3.10 Å (87); 30.11°, 2.97 Å (50); 31.96°, 2.80 Å (21)
Raman peaks (cm^{-1})	1121 M, 1037 W, *969 S*, 927 M sh, 284 M
$VOHPO_4 \cdot 4H_2O$	
XRD peaks 2Θ	11.95°, 7.40 Å (100); 13.64°, 6.49 Å (54); 16.34°, 5.42 Å (10); 21.17°, 4.19 Å (37); 22.05°, 4.03 Å (42); 22.94°, 3.87 Å (13); 26.46°, 3.37 Å (21); 27.43°, 3.25 Å (11); 31.20°, 2.86 Å (11); 31.97°, 2.80 Å (72); 33.47°, 2.68 Å (16)
Raman peaks (cm^{-1})	*1084 vS*, 1055 S sh, *998 vS*, 982 vS, 509 S, 402 M, 321 S, 266 vS, 215 W, 192 W, 166 W
$VO(H_2PO_4)_2$	
XRD peaks 2Θ	14.01°, 6.32 Å (90); 22.37°, 3.97 Å (57); 24.89°, 3.57 Å (85); 26.46°, 3.37 Å (30); 28.18°, 3.16 Å (100); 30.06°, 2.97 Å (20); 31.57°, 2.83 Å (73); 36.23°, 2.48 Å (28); 43.13°, 2.10 Å (58)
Raman peaks (cm^{-1})	1151 M br, *935 vS*, 900 M sh, 575 M, 224 M, 141 M
$(VO)_2P_2O_7$	
XRD peaks 2Θ	18.53°, 4.79 Å (10); 23.02°, 3.87 Å (100); 28.45°, 3.14 Å (60); 29.96°, 2.98 Å (28); 33.72°, 2.65 Å (8); 36.89°, 2.44 Å (10)
Raman peaks (cm^{-1})	1191 W, 1135 W, 1006 vW, 930 S sh, *920 vS*, 797 vW, 457 vW, 391 vW, 274 W, 258 W, 193 vW, 112 vW
γ-$VOPO_4$	
XRD peaks 2Θ	18.08°, 4.90 Å (93); 20.44°, 4.34 Å (55); 21.34°, 4.16 Å (85); 22.77°, 3.90 Å (83); 23.10°, 3.85 Å (100); 25.35°, 3.51 Å (89); 27.60°, 3.23 Å (51); 28.87°, 3.09 Å (81); 29.10°, 3.07 Å (85); 36.59°, 2.45 Å (44)
Raman peaks (cm^{-1})	1188 W, *1092 S*, 1036 M, 1018 M, 991 M sh, *945 vS*, 652 M, 634 M sh, 592 M, 554 W, 453 M, 410 M sh, 388 S, 356 M, 332 M, 291 M, 126 M
$VOPO_4 \cdot 2H_2O$	
XRD peaks 2Θ	12.03°, 7.35 Å (100); 18.71°, 4.74 Å (7); 24.12°, 3.69 Å (20); 28.82°, 3.10 Å (17); 31.30°, 2.86 Å (5); 39.32°, 2.29 Å (7)
Raman peaks (cm^{-1})	*1039 S*, 988 M, *952 vS*, 658 W, *542 S*, 451 W, 281 M, 198 W, 146 W
α_I-$VOPO_4$	
XRD peaks 2Θ	20.32°, 4.38 Å (8); 21.59°, 4.12 Å (60); 28.79°, 3.11 Å (100); 41.08°, 2.20 Å (40); 46.34°, 1.98 Å (20); 59.48°, 1.55 Å (18); 63.78°, 1.45 Å (15)
Raman peaks (cm^{-1})	1143 W, *1035 S*, 963 sh, 943 sh, *926 vS*, 661 W, 576 M, 539 M, 457 W, 429 W, 302 M, 291 M, 198 M, 171 M
$VO(PO_3)_2$	
XRD peaks 2Θ	22.42°, 2.95 Å (25); 23.09°, 3.84 Å (100); 24.22°, 3.67 Å (87); 27.24°, 3.27 Å (27); 27.71°, 3.21 Å (20); 29.03°, 3.07 Å (47); 30.70°, 2.91 Å (52); 34.24°, 2.62 Å (26); 45.72°, 1.98 Å (24); 47.33°, 1.91 Å (18)
Raman peaks (cm^{-1})	1271 M, *1255 S*, *1216 S*, 1109 W, 1065 W, *957 vS*, 692 M, 459 W, 397 W, 345 W, 259 W, 222 W, 207 W, 187 W, 130 W
$V(PO_3)_3$	
XRD peaks 2Θ	23.03°, 3.86 Å (100); 26.08°, 3.41 Å (40); 27.34°, 3.26 Å (10); 29.16°, 3.06 Å (16); 31.32°, 2.85 Å (10); 32.98°, 2.71 Å (19); 37.02°, 2.42 Å (14)
Raman peaks (cm^{-1})	*1229 S*, *1215 S*, 1180 M, 1127 W, 1070 W, 1020 W, *669 S*, 503 M, 420 M, 395 M, 368 W, 354 W, 292 W, 275 W, 244 M sh, 237 M, 172 W, 156 W, 131 W, 118 W

[a] Labels: vS = very strong, S = strong, M = medium, W = weak, sh = shoulder, br = broad.

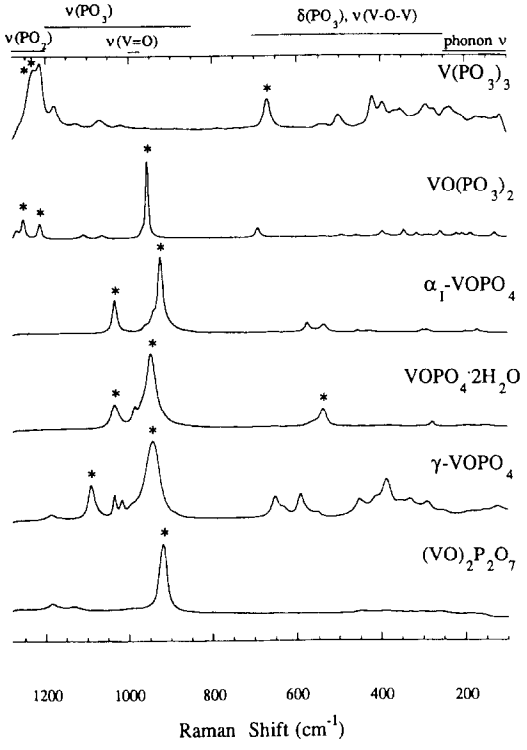

Fig. 4. Raman spectra of calcined reference VPO phases: $(VO)_2P_2O_7$, γ-$VOPO_4$, $VOPO_4 \cdot 2H_2O$, α_I-$VOPO_4$, $VO(PO_3)_2$ and $V(PO_3)_3$: * characteristic Raman bands.

about from the condensed phosphate structure. The polyphosphate $(PO_2)_n$ chains in the metaphosphates have a strong P–O stretch above 1200 cm^{-1} which can be used to distinguish vanadyl metaphosphate or vanadium trimetaphosphate [26].

The reference vanadyl phosphates have structures with different connectivity patterns of VO_6 octahedra and PO_4 tetrahedra. The most active catalysts are primarily vanadyl pyrophosphate, $(VO)_2P_2O_7$, which is derived from vanadyl hydrogen phosphate hemihydrate, $VOHPO_4 \cdot 0.5H_2O$. Vanadyl pyrophosphate is made up of sheets formed by the edge-sharing VO_6 pairs equatorially linked to pyrophosphate groups vanadyl pyrophosphate may be distinguished from orthophosphates and hydrogen phosphates by the presence of the symmetric P–O–P stretching band at 797 cm^{-1} (see Table 1). The bonding of the V = O to the structural water in vanadyl hydrogen phosphate hemihydrate increases the polarizability of the bond giving rise to V–O–P bands at 1109 and 1154 cm^{-1} that have stronger Raman intensity than in the pyrophosphate (see Figs. 3 and 4). The hemihydrate also has a very intense P–O band at 981 cm^{-1}, shifted to higher frequency than in the pyrophosphate.

The structures of α_I-$VOPO_4$ and its dihydrate, $VOPO_4 \cdot 2H_2O$, consist of isolated vanadyl octahedra that share an equatorial oxygen with one PO_4 tetrahedron and form V = O · · · V = O chains in perpendicular directions. The α_{II}- and β-VOPO4 structure differ in the specific orientation of the V = O relative to the PO_4 tetrahedra. The α_I-$VOPO_4$ Raman spectra is the simplest consisting primarily of a strong PO_4 band at 940 cm^{-1} and a strong V–O–P band at 1040 cm^{-1}. Additional bands are evident in the other phases due to structural distortions and intercalation of water (see Figs. 3 and 4 and Table 1). These bands are strong enough that they can be used to distinguish the different phases when they are present as minor constituents.

The Raman spectra of $VOHPO_4 \cdot 0.5H_2O$, $(VO)_2P_2O_7$, γ-, α_I-$VOPO_4$ and $VOPO_4 \cdot 2H_2O$ (Figs. 3 and 4) agreed well with the published data [14]. The correlation between the structures of these phases and Raman band assignments has been previously discussed [14]. A slight difference between the Raman spectra of vanadyl pyrophosphate of the present (Fig. 4) and previous study [14] has been observed. The Raman spectrum of the $(VO)_2P_2O_7$ obtained by dehydration at high temperature (973 K) displayed a 933 cm^{-1} band [14]. This band falls in the range of P–O stretches, it may be due to dehydration of P–OH groups at the surface of the vanadyl pyrophosphate. However, at typical catalytic reaction temperatures between 653 and 723 K the 933 cm^{-1} band was not observed in either reference $(VO)_2P_2O_7$ (Fig. 4 and Table 1) or the catalytic phases.

The structures of the dihydrogen phosphate, $VO(H_2PO_4)_2$, and metaphosphate, $VO(PO_3)_2$

are directly related [1,18]. The structural similarity is reflected in the Raman spectra, both compounds had a prominent phosphate stretch in the 930–970 cm^{-1} range (Figs. 3 and 4 and Table 1). Formation of the covalent $(PO_3)_n$ chains from the hydrogen-bonded H_2PO_4 tetrahedra resulted in the shift of the P–O stretch from 935 in $VO(H_2PO_4)$ to 957 cm^{-1} in $VO(PO_3)_2$. The polyphosphate structure in the $VO(PO_3)_2$ also resulted in Raman bands at 1216, 1255 and 1271 cm^{-1}.

The structure of $V(PO_3)_3$ is also built from the polyphosphate chains [27,28]. However, unlike vanadyl compounds, all the oxygen atoms in vanadium octahedra in the structure are shared with $(PO_3)_n$ and all V–O bond lengths are almost identical. Its Raman spectrum displayed weak features in the 1200–1000 cm^{-1} range corresponding to V–O–P stretches, and no peaks were present in the 1000–900 cm^{-1} range of the V = O stretch or PO_4 stretch (Fig. 4). The strong peaks at 1229 and 1215 cm^{-1} corresponded to ν_{as} of PO_2 groups observed in its IR spectrum (20).

α-$VOHPO_4 \cdot 2H_2O$ and $VOHPO_4 \cdot H_2O$ have layered structures with the layers held together by hydrogen bonding [29]. The Raman spectra of α-$VOHPO_4 \cdot 2H_2O$ and $VOHPO_4 \cdot H_2O$ demonstrate the structural similarity between the two phosphates (Fig. 3). The phosphate stretch shifts from 913 in α-$VOHPO_4 \cdot 2H_2O$ to 888 cm^{-1} in $VOHPO_4 \cdot H_2O$ probably as a result of slight differences in bond distances and angles within the HPO_4 tetrahedra in the two structures (Table 1).

The structures of $VOHPO_4 \cdot 4H_2O$ and β-$VOHPO_4 \cdot 2H_2O$ are closely related [30,31]. The Raman spectra of $VOHPO_4 \cdot 4H_2O$ and β-$VOHPO_4 \cdot 2H_2O$ prepared by the partial dehydration of $VOHPO_4 \cdot 4H_2O$ in air at 423 K (Fig. 3) are similar. The intercalated water molecules are lost; however, the coordination in both phosphates is largely unaffected, causing only a slight shift of the phosphate stretch (Fig. 3 and Table 1). The weak 912 and 888 cm^{-1} bands observed in the Raman spectrum of $VOHPO_4 \cdot 4H_2O$ probably come from the micro-crystalline α-$VOHPO_4 \cdot 2H_2O$ and $VOHPO_4 \cdot H_2O$ impurity phases, respectively.

3.2. Aqueous catalysts

XRD patterns set of VPO precursors and catalysts with synthesis P/V = 1.0 and 1.7 prepared in aqueous medium are shown in Figs. 5 and 6 and the corresponding Raman spectra are shown in Figs. 7 and 8.

For P/V = 1.0 the initial precursor is primarily the hemihydrate phase, $VOHPO_4 \cdot 0.5H_2O$. The XRD pattern and Raman spectrum of A:P:I:1.0 (Fig. 5a and Fig. 7a, respectively) both correspond to $VOHPO_4 \cdot 0.5H_2O$. The small XRD peaks at $2\Theta = 32.6°$ ($d = 2.74$ Å) and 23.0° ($d = 3.86$ Å) and the 913 cm^{-1} Raman band suggest trace amounts of α-$VOHPO_4 \cdot 2H_2O$ in the hemihydrate. A purified precursor A:P:II:1.0 was prepared by rinsing the initial precursor with boiling water to remove α-$VOHPO_4 \cdot 2H_2O$, which is slightly water-soluble. The XRD pattern of A:P:II:1.0 (Fig. 5a) showed no evidence of the α-dihydrate, however the Raman spectrum (Fig. 7a) showed a residual peak at 911 cm^{-1} indicating a remnant of the α-dihydrate not detected by XRD.

The water-soluble components of the initial catalyst precursor were recovered by evaporation of the solvent as sample A:P:III:1.0. The XRD pattern of precursor III (the water-soluble components) in Fig. 5a corresponds to a mixture of NH_4Cl (peaks at $2\Theta = 23.2$, 32.8, 40.4 and 47.1°), $VOHPO_4 \cdot H_2O$ (13.0, 26.2, 28.6, 31.5 and 35.9°), α-$VOHPO_4 \cdot 2H_2O$ (24.3, 37.8 and 39.2°), possibly α_I-$VOPO_4$ (28.6, 45.9 and 47.1°) [1,2,18] and $VOHPO_4 \cdot 0.5H_2O$ (15.7 and 24.3°). The Raman spectrum of precursor III (Fig. 7a) is diffuse and most of the band positions are shifted some 5–10 cm^{-1} from those reported for the reference VPO phases. Raman spectroscopy is not very sensitive to the ammonium chloride, which was the primary species detected by XRD. The strongest band at 865 cm^{-1} is characteristic of $VOHPO_4 \cdot H_2O$. The

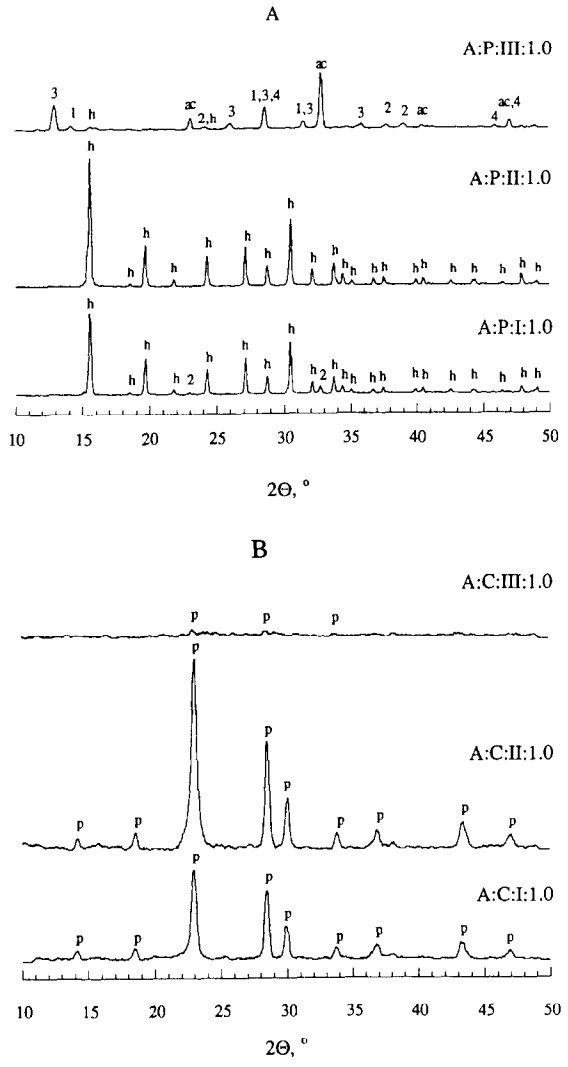

Fig. 5. XRD patterns of aqueous P/V = 1 precursors (a) and catalysts I–III (b): (a) A:P:I:1.0, precursor I evaporated from the V(IV)/H_3PO_4 reaction mixture; A:P:II:1.0, precursor II, a water insoluble component of precursor I; A:P:III:1.0, precursor III, a water soluble component of precursor I; (b) A:C:I:1.0, A:C:II:1.0 and A:C:III:1.0 are catalysts I, II and III, respectively, obtained by calcination of the precursors at 823 K in nitrogen for 2 h. h = $VOHPO_4 \cdot 0.5H_2O$, ac = NH_4Cl, 1 = $VO(H_2PO_4)_2$, 2 = α-$VOHPO_4 \cdot 2H_2O$, 3 = $VOHPO_4 \cdot H_2O$, 4 = α_I-$VOPO_4$, p = $(VO)_2P_2O_7$, 5 = $VOPO_4 \cdot 2H_2O$, 6 = $VO(PO_3)_2$, 7 = $V(PO_3)_3$, 8 = β-$VOPO_4$, 9 = δ-$VOPO_4$, 10 = γ-$VOPO_4$, 11 = α_{II}-$VOPO_4$.

weak Raman bands for A:P:III:1.0 indicate the presence of other VPO phases, possibly $VO(H_2PO_4)_2$ (the unshifted 936 cm^{-1} band), $VOPO_4 \cdot 2H_2O$ and/or α_I-$VOPO_4$ (bands at 1016, 990, 693, 565, 535, 453, 277 and 151 cm^{-1}), and possibly $VOHPO_4 \cdot 0.5H_2O$ (990 cm^{-1}). The hydrated phase, $VOPO_4 \cdot 2H_2O$, is most likely considering the experimental conditions employed (boiling in water).

At the higher synthetic P/V ratio of 1.7, both XRD and Raman results (Fig. 6a and Fig. 8a) indicated that the precursor A:P:I:1.7 consisted predominantly of $VO(H_2PO_4)_2$ and lesser amounts of $VOHPO_4 \cdot 0.5H_2O$. The relative

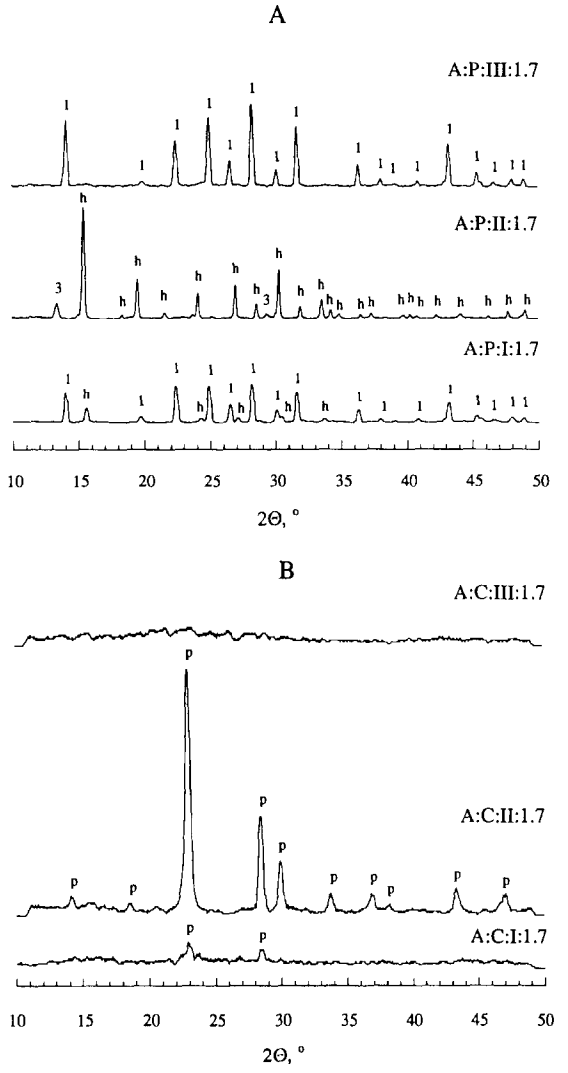

Fig. 6. XRD patterns of aqueous P/V = 1.7 precursors (a) and catalysts I–III (b): (a) A:P:I:1.7, precursor I; A:P:II:1.7, precursor II; A:P:III:1.7, precursor III; (b) A:C:I:1.7, catalyst I; A:C:II:1.7, catalyst II; A:C:III:1.7, catalyst III. The same system of labeling as in Fig. 5.

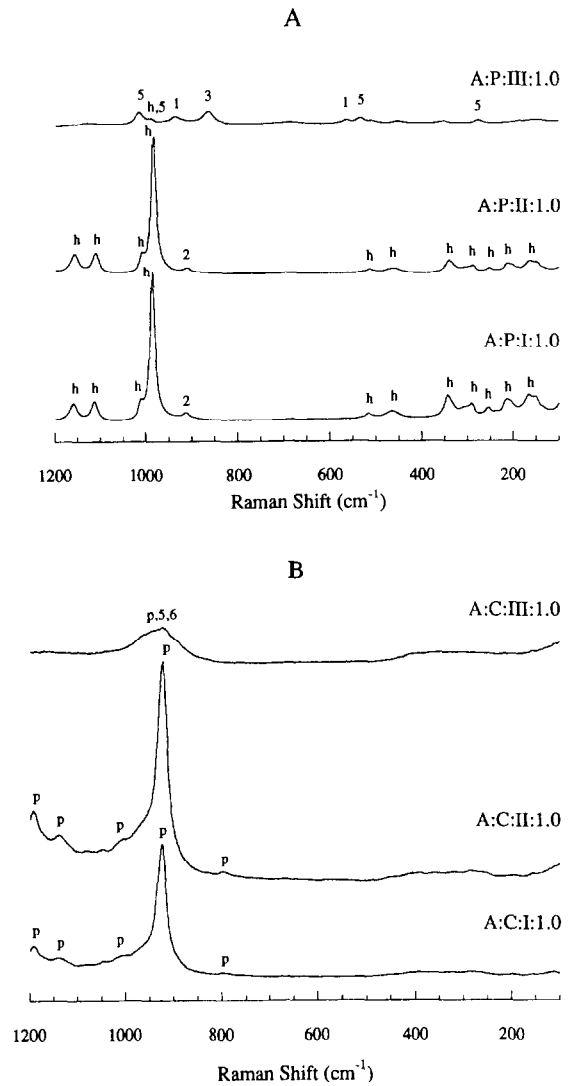

Fig. 7. Raman spectra of aqueous P/V = 1 precursors (a) and catalysts I–III (b): (a) A:P:I:1.0, precursor I; A:P:II:1.0, precursor II; A:P:III:1.0, precursor III; (b) A:C:I:1.0, catalyst I; A:C:II:1.0, catalyst II; A:C:III:1.0, catalyst III. The same system of labeling as in Fig. 5.

amounts of $VOHPO_4 \cdot 0.5H_2O$ (30.6%) and $VO(H_2PO_4)_2$ (69.4%) in precursor I based on intensities of their respective (001) and (220) reflections [32] are in excellent agreement with the values of 30 and 70% expected from the synthetic P/V ratio of 1.7 used. Boiling water removed the $VO(H_2PO_4)_2$, and the remaining component, A:P:II:1.7, consisted mostly of $VOHPO_4 \cdot 0.5H_2O$ with traces of $VOHPO_4 \cdot H_2O$ (XRD peaks at $2\Theta = 13.5$ and 29.5° and the Raman band at 880 cm^{-1}) and α-$VOHPO_4 \cdot 2H_2O$ (Raman band at 911 cm^{-1}). Raman spectroscopy provided more information about the phase composition of the water-soluble precursor, A:P:III:1.7, than XRD. XRD only indicated $VO(H_2PO_4)_2$; Raman spectroscopy detected small amounts of α-$VOHPO_4 \cdot 2H_2O$, $VOHPO_4 \cdot H_2O$, some $VOPO_4$ phase (either α_I- or dihydrate), and possibly $VOHPO_4 \cdot 0.5H_2O$ in addition to $VO(H_2PO_4)_2$. α_I-$VOPO_4$ or di-

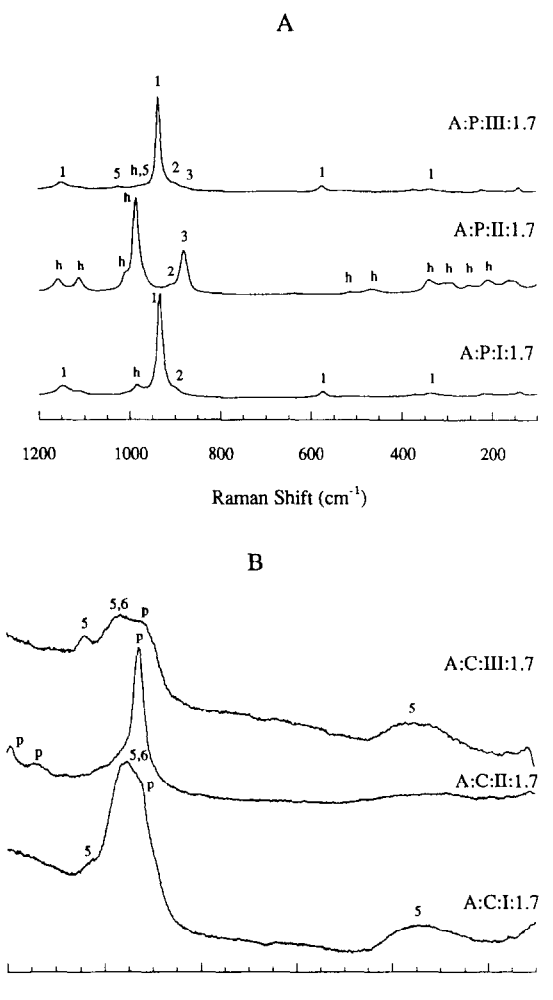

Fig. 8. Raman spectra of aqueous P/V = 1.7 precursors (a) and catalysts I–III (b): (a) A:P:I:1.7, precursor I; A:P:II:1.7, precursor II; A:P:III:1.7, precursor III; (b) A:C:I:1.7, catalyst I; A:C:II:1.7, catalyst II; A:C:III:1.7, catalyst III. The same system of labeling as in Fig. 5.

hydrate is seen at 1024 cm^{-1} and possibly as a shoulder at 980 cm^{-1}, the α-dihydrate and monohydrate as shoulders at 900 and 880 cm^{-1}, respectively, and $VOHPO_4 \cdot 0.5H_2O$ at 980 cm^{-1}.

XRD patterns and Raman spectra of the P/V = 1 catalysts derived from aqueous synthesis, A:C:I:1.0 and A:C:II:1.0 shown in Fig. 5b and Fig. 7b, correspond to vanadyl(IV) pyrophosphate, with no evidence of $VOPO_4$ phases. Catalyst A:C:III:1.0 (from the water-soluble precursor) is XRD amorphous with the exception of two weak peaks at 2Θ of ca. 23.0 and 28.4° corresponding, respectively, to the most intense (020) and (204) reflections in the XRD pattern of vanadyl pyrophosphate. The Raman spectrum of catalyst III is characteristic of a poorly ordered vanadyl pyrophosphate. The presence of $VO(PO_3)_2$ (961 cm^{-1}) and a number of $VOPO_4$ phases can not be excluded in view of the broad spectral feature in the 930–970 cm^{-1} region.

At high P/V ratio the resulting catalysts have less crystalline order. A:C:I:1.7 is almost amorphous in XRD (Fig. 5b) with exception of two weak peaks at 2Θ of 22.97 and 28.38° corresponding, respectively, to the most intense (020) and (204) reflections of vanadyl pyrophosphate. The corresponding Raman spectrum (Fig. 8b), showed a broad feature in 920–970 cm^{-1} region, consisting of at least two components at ca. 955 cm^{-1} (corresponding to $VO(PO_3)_2$ and possibly $VOPO_4 \cdot 2H_2O$) and 923 cm^{-1} (corresponding to vanadyl pyrophosphate). The very broad Raman band centered at ca. 350 cm^{-1} suggests the possibility of $VOPO_4$. The water-insoluble precursor enriched in vanadyl hydrogen phosphate hemihydrate produced a catalyst, A:C:II:1.7 that is almost exclusively vanadyl pyrophosphate. The catalyst from the water soluble precursors A:C:III:1.7 is XRD amorphous. Its Raman spectrum possesses the 1038 cm^{-1} band characteristic of α_I-$VOPO_4$ and/or $VOPO_4.2H_2O$ and the broad feature in the 900–980 cm^{-1} region, which could result from $VO(PO_3)_2$ (961 cm^{-1} band), $VOPO_4 \cdot 2H_2O$ (954 cm^{-1}), or vanadyl pyrophosphate (922 cm^{-1}). The broad feature at ca. 350 cm^{-1} again suggests the presence of some $VOPO_4$ phase.

The kinetic studies of the catalysts from the aqueous synthesis route and the reference $VO(H_2PO_4)_2$ phase are summarized in Table 2. BET surface areas of the VPO catalysts are also given in Table 2. The catalysts that were principally vanadyl pyrophosphate (A:C:I:1.0, A:C:II:1.0, A:C:I:1.7, A:C:II:1.7) exhibited selectivities to maleic anhydride in the 53–56% range at 86–87% *n*-butane conversion, while the catalyst from water soluble precursor A:C:III:1.0, which contained orthophosphates was less selective (20%). The catalyst obtained from a water soluble precursor at the high P/V ratio, A:C:III:1.7, had a very low surface area and the conversion of *n*-butane, even at small space velocities, was low. The selectivity for maleic anhydride was comparable to vanadyl pyrophosphate, which existed as a minor component in this catalyst. The kinetic tests of

Table 2
Performance of the aqueous catalysts and reference $VO(H_2PO_4)_2$ phase in *n*-butane oxidation at 723 K in 1.2% *n*-butane in air

Catalyst	BET surface area (m^2/g)	GHSV (h^{-1})	Conversion (mol%)	Selectivity (mol%)	R [a] 10^{-5} (mol h^{-1} m^{-2})
A:C:I:1.0	5.3	750	86	53	19.3
A:C:II:1.0	8.3	750	87	56	18.3
A:C:III:1.0	2.7	3400	25	20	20.9
A:C:I:1.7	1.7	800	8	67	19.1
A:C:II:1.7	3.0	750	24	58	18.6
A:C:III:1.7	0.5	200	6	72	1.3
$VO(H_2PO_4)_2$	0.3	200	0		0

[a] The rate of *n*-butane oxidation.

$VO(H_2PO_4)_2$, which converts into $VO(PO_3)_2$ under reaction conditions, shows the complete inertness of $VO(PO_3)_2$ toward hydrocarbon activation (Table 2).

XRD patterns and Raman spectra obtained on the catalysts after 150 h on-line in the reactor are shown in Fig. 6b and Fig. 8b. The catalysts that were principally $(VO)_2P_2O_7$ initially (A:C:I:1.0, A:C:II:1.0 and A:C:II:1.7) did not show any significant changes after reaction. Those catalysts from the water soluble residues of the aqueous precursors, A:C:III:1.0 and A:C:III:1.7, showed crystallization after 150 h under reaction conditions. The P/V = 1 catalyst, A:C:III:1.0, showed formation of crystalline $(VO)_2P_2O_7$, β-, δ- and γ-$VOPO_4$. The P/V = 1.7 catalyst, A:C:III:1.7, showed crystal growth of V(IV) metaphosphate, $VO(PO_3)_2$, with trace amounts of vanadyl pyrophosphate and vanadium trimetaphosphate, $V(PO_3)_3$.

^{31}P spin-echo NMR spectra of $VO(H_2PO_4)_2$, $VO(H_2PO_4)_2$ calcined at 773 K in air for 1 h, $V(PO_3)_3$, and the $VO(H_2PO_4)_2$ catalyst are shown in Fig. 9. The NMR spectrum of $VO(H_2PO_4)_2$ contained a broad feature centered around 2100 ppm (Fig. 9). The XRD pattern agreed with the one reported by Villeneuve et al. [18]. After calcination in air at

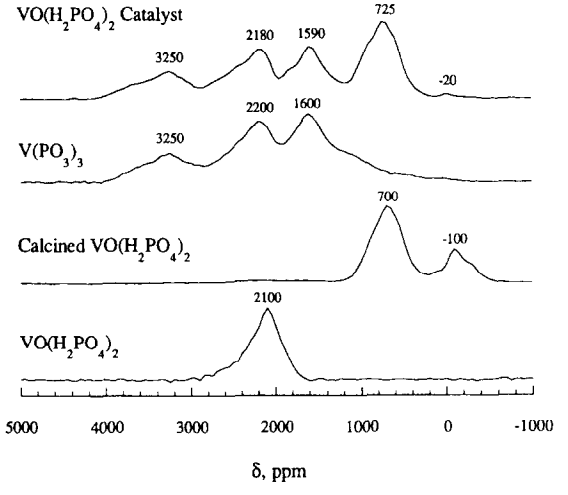

Fig. 9. ^{31}P spin echo NMR spectra of reference $VO(H_2PO_4)_2$, $VO(H_2PO_4)_2$ calcined at 773 K in air for 1 h, reference $V(PO_3)_3$, and $VO(H_2PO_4)_2$ catalyst.

773K for 1 h, the XRD pattern and Raman spectrum of the solid were those of crystalline $VO(PO_3)_2$ containing traces of $V(PO_3)_3$, while the NMR spectrum displayed broad peaks at 700 and −100 ppm (Fig. 9), which we ascribed to $VO(PO_3)_2$ and V(V) dispersed in the $VO(PO_3)_2$ matrix, respectively. The $V(PO_3)_3$ phase displayed peaks at 1600, 2200 and 3250 ppm in its ^{31}P NMR spectrum (Fig. 9). The NMR spectrum of catalyst A:C:III:1.7, derived from the water soluble precursors, displayed peaks at −20, 1590, 2180 and 3250 ppm from $V(PO_3)_3$ in addition to the 725 ppm peak of vanadyl metaphosphate, $VO(PO_3)_2$ [16].

3.3. Organic catalysts

The XRD patterns of the precursors derived from organic solvent (O:P:1.18 and O:P:1.5), fresh catalysts (O:C:I:1.18 and O:C:I:1.5), catalysts after 150 h on-line in the reactor (O:C:II:1.18 and O:C:II:1.5), and the corresponding orthophosphate phases after high temperature oxidation (O:C:III:1.18 and O:C:III:1.5) are shown in Fig. 10. The Raman spectra are shown in Fig. 11 (the spectra of the hemihydrate precursors are not included due to strong fluorescence). The XRD patterns of the precursors showed only the hemihydrate. There are some differences in the relative intensities of the diffraction peaks in the precursors at the two different P/V ratios, but there was no evidence for other phases. After calcination at 823 K in nitrogen and after 150 h on-line in the butane–air reaction mixture both the XRD and Raman spectra of the catalysts were indicative of only $(VO)_2P_2O_7$. However, the catalysts prepared at P/V ratio of 1.18 show a much more intense diffraction peak at $2\Theta = 23°$ corresponding to the (020) direction, suggesting that the ordering of the layers in the pyrophosphate is dependent on the P/V ratio.

The pyrophosphate catalysts were converted to orthophosphates by high temperature oxidation to see if differences in catalyst composition at two P/V ratios could be further ascertained

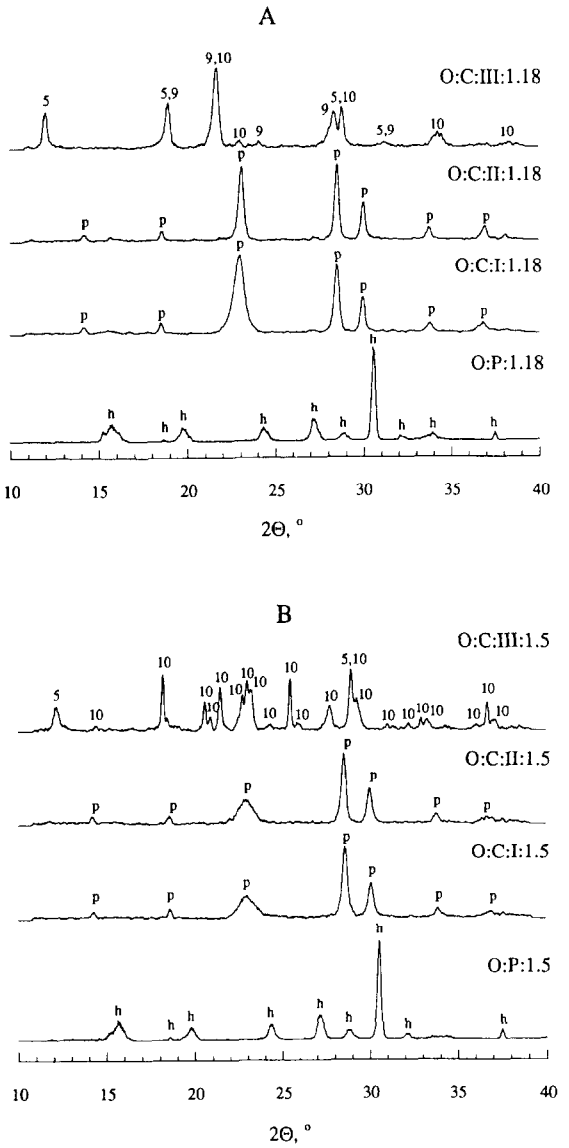

Fig. 10. Powder X-ray diffraction patterns of the organic VPO system at P/V ratios of 1.18 (a) and 1.5 (b): (a) O:P:1.18, a precursor phase possessing synthetic P/V = 1.18; O:C:I:1.18, the P/V = 1.18 catalyst before kinetic studies; O:C:II:1.18, the P/V = 1.18 catalyst after kinetic studies; O:C:III:1.18, the P/V = 1.18 orthophosphate phase produced by complete oxidation of O:C:I:1.18; (b) O:C:I:1.5, the P/V = 1.5 catalyst before kinetic studies; O:C:II:1.5, the P/V = 1.5 catalyst after kinetic studies; O:C:III:1.5, the P/V = 1.5 orthophosphate phase produced by complete oxidation of O:C:I:1.5. The same system of labeling as in Fig. 5.

from this phase transformation. The XRD pattern of O:C:III:1.18 displayed peaks of $VOPO_4 \cdot 2H_2O$ (12.00, 18.92, and 28.76°), γ-$VOPO_4$(21.66, 28.76, and 34.22°) and δ-$VOPO_4$ (18.92, 21.66, and 28.30°). The Raman spectra indicated that O:C:III:1.18 contained δ-$VOPO_4$ (1082, 1019 and 931 cm^{-1}) and some β-$VOPO_4$ (983, 893 and 432 cm^{-1}). XRD of the or-

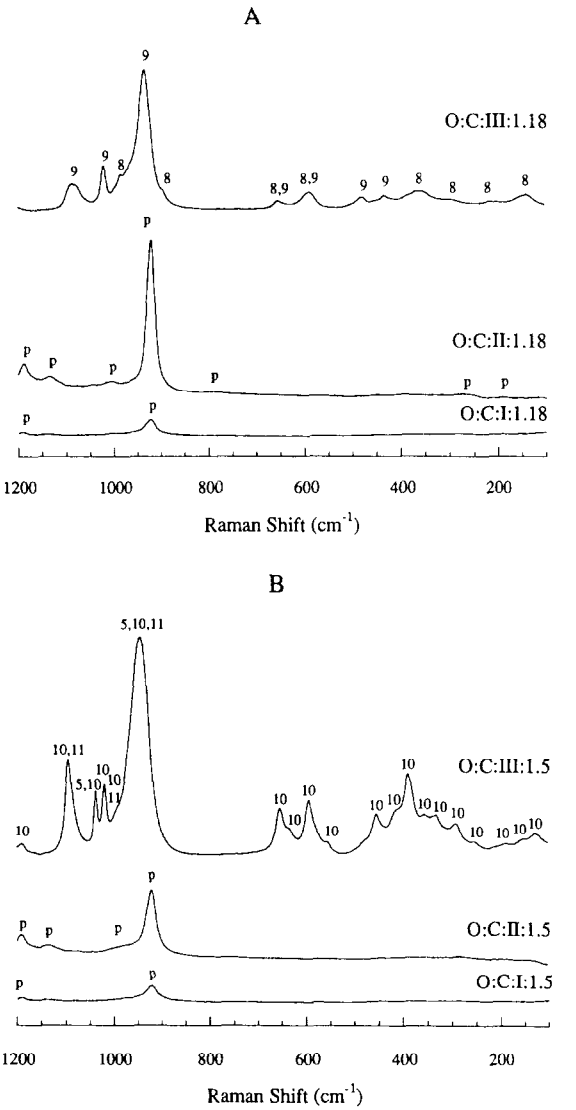

Fig. 11. Raman spectra of the organic VPO catalysts at P/V ratios of 1.18 (a) and 1.5 (b): (a) O:C:I:1.18, the P/V = 1.18 catalyst before kinetic studies; O:C:II:1.18, the P/V = 1.18 catalyst after kinetic studies; O:C:III:1.18, the P/V = 1.18 orthophosphate phase produced by complete oxidation of O:C:I:1.18; (b) O:C:I:1.5, the P/V = 1.5 catalyst before kinetic studies; O:C:II:1.5, the P/V = 1.5 catalyst after kinetic studies; O:C:III:1.5, the P/V = 1.5 orthophosphate phase produced by complete oxidation of O:C:I:1.5. The same system of labeling as in Fig. 5.

thophosphate with P/V of 1.5, O:C:III:1.5, showed the presence of $VOPO_4 \cdot 2H_2O$ (12.07, 23.09, and 28.84°) and γ-$VOPO_4$ (18.11, 20.49, 21.37, 22.64, 22.89, 25.39, 28.84, 29.12 and 36.62°). The Raman spectrum of O:C:III:1.5 indicated $VOPO_4 \cdot 2H_2O$ (1038, 991 and broad peak at 943 cm^{-1}) and γ-$VOPO_4$ (1189, 1094, 1038, 1019, 991 and 943 cm^{-1}), and possibly some α_{II}-$VOPO_4$ (1094, 991 and 943 cm^{-1}).

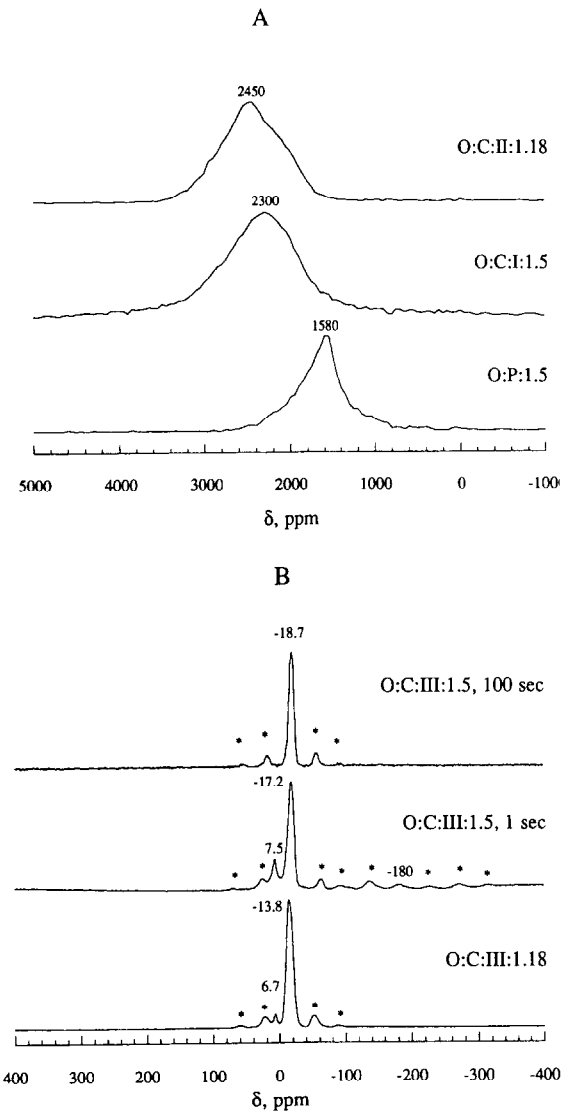

Fig. 12. (a) ^{31}P spin echo NMR spectra of paramagnetic organic VPO phases: O:P:1.5, precursor with P/V = 1.5; O:C:I:1.5, the catalyst with P/V = 1.5; O:C:II:1.18, catalyst with P/V = 1.18 after kinetic studies. (b) ^{31}P MAS-NMR spectra of the diamagnetic organic VPO phases: O:C:III:1.18 (P/V = 1.18 orthophosphate) and O:C:III:1.5 (P/V = 1.5 orthophosphate) collected at relaxation delay times of 1 and 100 s: * rotation side bands.

Table 3
Performance of the organic catalysts O:C:I:1.18 and O:C:I:1.5 in *n*-butane oxidation to maleic anhydride at 708 K in 1.2% *n*-butane in air

Catalyst	BET surface area (m^2/g)	GHSV (h^{-1})	Conversion (mol%)	MA selectivity (mol%)
O:C:I:1.18	22.5	1250	80	66
O:C:I:1.5	15.3	750	78	52

The ^{31}P spin-echo and MAS-NMR spectra of the organically derived precursors and catalysts are shown in Fig. 12. The spectrum of O:P:1.5 exhibited a single peak at 1580 ppm. Calcination in nitrogen produced vanadyl pyrophosphate catalyst (O:C:I:1.5), which displayed a single peak at 2300 ppm [16]. The ^{31}P NMR spectrum of the catalyst produced from the P/V = 1.18 precursor, O:C:I:1.18, had a similar ^{31}P NMR spectrum but the peak was shifted upfield to 2450 ppm and showed some distortion suggesting it was comprised of more than a single peak. Calcination of both catalysts in oxygen at 1073 K converted them into diamagnetic V(V) orthophosphate phases O:C:III:1.18 and O:C:III:1.5 (Figs. 10 and 11). ^{31}P MAS-NMR spectra of these materials were collected (Fig. 12b). The spectrum of O:C:III:1.18 exhibited peaks of δ-$VOPO_4$ at −13.8 ppm and $VOPO_4 \cdot 2H_2O$ at 6.7 ppm [33]. This spectrum was not dependent on the time delay from the rf pulse and the acquisition of the FID. The ^{31}P MAS-NMR of the orthophosphate phase at the higher P/V ratio, O:C:III:1.5 was dependent of the relaxation delay time. At short relaxation delays (1–2 s), the spectrum of O:C:III:1.5 displayed the large peak at −17.2 ppm indicative of γ-$VOPO_4$ [33], a smaller peaks of $VOPO_4 \cdot 2H_2O$ at 7.5 ppm and a peak from some unidentified diamagnetic phase at −180 ppm. At longer delays (100 s), only the peak of γ-$VOPO_4$ at −18.7 ppm was observed.

Surface area measurements and kinetic tests for *n*-butane oxidation to maleic anhydride of both pyrophosphate catalysts, O:C:I:1.18 and

Table 4
Model organic VPO catalysts

VPO material	I_{200}/I_{042} [a]	(200) FWHM [b] (°)	(042) FWHM [c] (°)
M:P:A	2.35	0.17	0.13
M:P:B	2.67	0.13	0.12
M:C:I:A	1.09	1.02	0.32
M:C:II:A	0.98	0.50	0.35
M:C:III:A	4.23	0.76	0.29
M:C:I:B	1.29	0.76	0.32
M:C:II:B	1.17	0.52	0.25
M:C:III:B	4.23	0.73	0.23

For precursors: [a] I_{001}/I_{130}. [b] (001) reflection. [c] (130) reflection.

O:C:I:1.5, were carried out (Table 3). The catalyst with P/V ratio 1.18 (O:C:I:1.18) performed very similarly to the unpromoted commercial organic catalysts [9], while the catalyst with the higher P/V ratio, O:C:I:1.5 was less active and less selective. The catalyst with the higher P/V ratio had a lower surface area which accounts in part for the lower catalytic activity.

3.4. Model organic catalysts

XRD patterns and Raman spectra of the precursors and catalysts of the model organic catalysts displaying platelet morphology were obtained after 2 (sample A) and 24 (sample B) h reduction periods. The XRD of the two precursors, M:P:A and M:P:B were identical showing only the vanadyl hemihydrate phase, $VOHPO_4 \cdot 0.5H_20$. Crystalline order as measured by the ratio of XRD intensities I_{200}/I_{042} and the peak widths is reported in Table 4. The Raman spectra of the two catalyst precursors are shown in Figs. 13 and 14 are those of $VOHPO_4 \cdot 0.5H_2O$ with trace amounts of α-$VOHPO_4 \cdot 2H_2O$, seen as a weak band at 913 cm^{-1}.

The precursors calcined in nitrogen gave rise to vanadyl pyrophosphate (catalysts M:C:I:A and M:C:I:B) of relatively low crystallinity (Table 4). The Raman spectra of M:C:I:A and M:C:I:B (Figs. 13 and 14) showed only a weak vanadyl pyrophosphate band at 924 cm^{-1} indicative of poor crystallinity. After calcination in oxygen an additional peak at $2\Theta = 21.33°$ (4.16 Å) was observed in the XRD patterns of

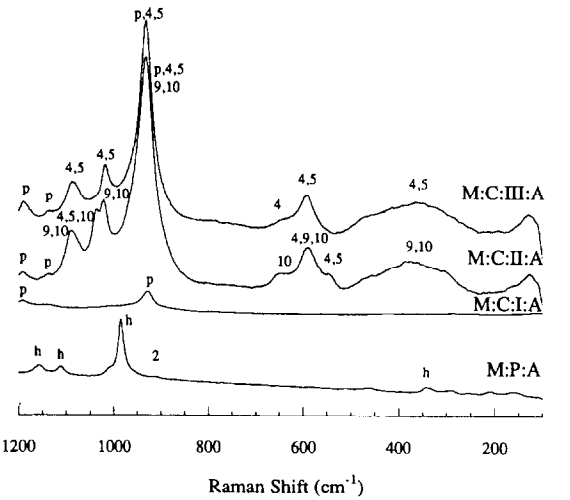

Fig. 13. Raman spectra of the model organic VPO system: M:P:A, precursor obtained after reduction in refluxing 2-butanol for 2 h; M:C:I:A, precursor M:P:A calcined in nitrogen at 823 K for 2 h; M:C:II:A, obtained by calcination of catalyst M:C:I:A at 773 K in oxygen for 2 h; M:C:III:A, obtained by washing catalyst M:C:II:A with water. The same system of labeling as in Fig. 5.

both catalysts suggesting the presence of γ-$VOPO_4$ [1]. The crystallinity of vanadyl pyrophosphate improved due to calcination in oxygen, as evidenced by the smaller (200) FWHM values, while the stacking order reflected by the

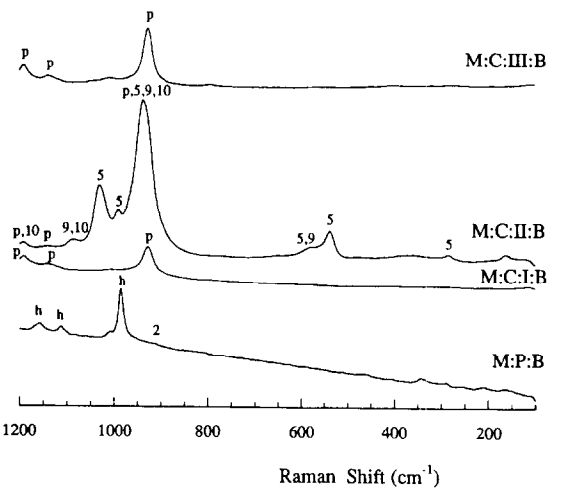

Fig. 14. Raman spectra of the model organic VPO system: M:P:B, precursor obtained after reduction in refluxing 2-butanol for 24 h; M:C:I:B, precursor M:P:A calcined in nitrogen at 823 K for 2 h; M:C:II:B, obtained by calcination of catalyst M:C:I:B at 773 K in oxygen for 2 h; M:C:III:B, obtained by washing catalyst M:C:II:B with water. The same system of labeling as in Fig. 5.

I_{200}/I_{042} ratio remained relatively unchanged (Table 4). The PO_4 band and other features in the Raman spectra of the catalysts calcined in air were more intense in accordance with the higher X-ray crystalline order. The Raman spectra showed a broad spectral feature between 920–960 cm^{-1} indicating the presence of orthophosphate phases (α_I-, δ-, γ-$VOPO_4$ and possibly $VOPO_4 \cdot 2H_2O$) as well as pyrophosphate (see Figs. 13 and 14).

The orthophosphate species in the oxygen calcined catalysts were removed by water and the remaining catalysts, M:C:III:A and M:C:III:B, showed increased crystallinity of vanadyl pyrophosphate. Considerable improvement in stacking order of the pyrophosphate was observed in M:C:III:A and M:C:III:B, while the increase in (200) FWHM values suggested thinner platelet particles (Table 4). Although the XRD results indicated the removal of the crystalline γ-$VOPO_4$ after the water treatment, Raman data unambiguously showed that some amorphous $VOPO_4$ still remained (Figs. 13 and 14). Catalyst M:C:III:A was principally vanadyl pyrophosphate, but δ-orthophosphate and γ-orthophosphate were also evident in the Raman spectrum, whereas the Raman spectrum of catalyst M:C:III:B indicated almost pure vanadyl pyrophosphate. An independent test demonstrated that additional water treatment of M:C:III:A removed residual V(V) species completely.

Reaction kinetics of the B catalysts in 1.2% *n*-butane in air at 673 K were monitored as a function of time. (The B catalysts were more fully reduced during the synthesis and were take as representative of the model organic VPO system.) Steady state was achieved after ca. 120 h on stream. The selectivity to maleic anhydride at 50% *n*-butane conversion increased from 44 to 58% over a period of 5 days. Removal of the soluble $VOPO_4$ phases led to considerable increase in surface area of catalyst M:C:III:B (Table 5). Raman spectra of the catalysts M:C:I:B and M:C:III:B collected after the kinetic studies were virtually unchanged from the fresh catalysts. In catalyst M:C:II:B the $VOPO_4 \cdot 2H_2O$ was converted to α_I-$VOPO_4$ so the used catalyst consisted of vanadyl pyrophosphate, along with lesser amounts of α_I-$VOPO_4$, δ-$VOPO_4$ and γ-$VOPO_4$. The ^{31}P spin-echo NMR spectrum of catalyst M:C:III:B showed a single peak at 2420 ppm corresponding to vanadyl pyrophosphate [16].

Table 5
Catalytic performance of catalysts M:C:B at 673 K in 1.2% *n*-butane in air: *n*-butane conversion and selectivity to maleic anhydride

Catalyst	BET surface area (m^2/g)	GHSV (h^{-1})	Conversion (mol%)	Selectivity (mol%)
M:C:I:B	9.0	1200	19	53
M:C:II:B	5.9	720	24	22
M:C:III:B	31.5	2100	50	58

4. Discussion

Correlation of the results of kinetic studies with bulk composition of VPO catalysts determined by XRD has led to the conclusion that the best catalysts for *n*-butane oxidation to maleic anhydride contain only highly crystalline vanadyl pyrophosphate. However, different synthesis routes to obtain vanadyl pyrophosphate produce catalysts with variable performance. The variability in performance is a result of the presence of other VPO phases, different microstructure, and different morphology. Evidence existing in the literature suggests that such reaction parameters as the solvent used during reduction of the V(V), and the P/V ratio dramatically affect the morphology, crystalline content, and the formation of amorphous VPO phases [5]. The present study was undertaken to show how the use of spectroscopic techniques of VPO catalysts can complement and extend our knowledge of their structure, and illuminate the critical features in preparing the best catalysts in a reproducible fashion.

The Raman and XRD results presented here for model VPO compounds are in good agree-

ment with previous results presented by Volta and co-workers [14]. We have extended their work by also examining the metaphosphate phases, $VO(PO_3)_2$ and $V(PO_3)_3$ which we found were formed during calcination of vanadyl(IV) dihydrogen phosphate, $VO(H_2PO_4)_2$. The vanadium metaphosphate species were found to form from aqueous precursors with P/V ratios greater than 1.0. These phases are catalytically inactive and hence degrade the performance of the catalysts.

4.1. Aqueous catalysts

The precursors with a P/V = 1.0 derived from aqueous media were principally vanadium hydrogen phosphate hemihydrate, but vanadyl(IV) hydrogen phosphate mono- and dihydrates were identified as impurities. At high P/V ratios the hemihydrate content in the precursor decreased and the formation of vanadium(IV) dihydrogen phosphate was preferred. Our data suggest that the fraction of the VPO as hemihydrate scaled with synthesis P/V ratio, going from one at P/V = 1.0 to zero at P/V = 2.0.

The hemihydrate phase converts to vanadyl pyrophosphate upon calcination at 823 K in nitrogen. XRD results for the catalysts from the aqueous precursors showed that the crystalline order of the pyrophosphate decreased with the content of the dihydrogen phosphate. The broad features in the Raman spectra between 900–980 cm^{-1} indicated that the amorphous component of the catalysts contained vanadyl dihydrogen phosphate, vanadyl metaphosphate and some orthophosphate phase(s). At the high P/V ratio of 1.7 the vanadyl dihydrogen phosphate was converted to vanadyl metaphosphate by calcination with the loss of water.

$$VO(H_2PO_4)_2 \rightarrow VO(PO_3)_2 + 2H_2O$$

Formation of the amorphous intermediate phases during the thermal transformation of $VOHPO_4 \cdot 0.5H_2O$ and $VO(H_2PO_4)_2$ has been previously suggested [30]. The complete conversion to crystalline vanadyl pyrophosphate occurs only after prolonged heating at high temperatures. Joining of (H_2PO_4) groups into the infinite metaphosphate $(PO_3)_n$ chains to explain formation requires significant lattice disruption which may produce an amorphous phase during the thermal transformation of $VO(H_2PO_4)_2$ [30].

At higher temperatures and longer heating times, reduction of the metaphosphate occurs ($V^{4+} \rightarrow V^{3+}$) accompanied by evolution of O_2, and the light green V(III) trimetaphosphate, $V(PO_3)_3$, precipitates [19,20]. We observed formation of $V(PO_3)_3$ in the $VO(PO_3)_2$ system, when the bulk P/V ratio was fixed. Polyphosphate features as found in $V(PO_3)_3$ were observed by NMR (see Fig. 9) in the aqueous VPO system (A:C:III:1.7 after kinetic studies) and the dihydrogen phosphate catalyst. When P/V ratio is less than 3, formation of V(III) trimetaphosphate (P/V = 3) may be accompanied by the formation of an orthophosphate phase (P/V = 1):

$$V^{4+}(P/V = 2) \rightarrow V^{3+}(P/V = 3) + V^{5+}(P/V = 1)$$

The peak in the diamagnetic range (−200 to 0 ppm) observed in the ^{31}P spin-echo NMR spectra of the paramagnetic metaphosphate phases (Fig. 9) may be an indication of some V(V) orthophosphate.

The kinetic studies of *n*-butane oxidation showed that the product slate stabilized after 100–150 h at 723 K in the reactive feed. Crystallization of the amorphous components of the catalyst appeared to be nearly complete after 150 h. The catalysts containing orthophosphate phases had comparable activities to pyrophosphate catalysts but were less selective. The metaphosphate phases, $VO(PO_3)_2$ and $V(PO_3)_3$, were inactive for *n*-butane oxidation at 723 K. Correlation of catalytic performance with phase composition of the aqueous VPO catalysts indicated that, contrary to previous suggestions [1,7,8,16], vanadium(IV) metaphosphate and the various orthophosphate ($VOPO_4$) phases are not

involved in the selective oxidation of *n*-butane. The experimental evidence presented here supports the hypothesis [6] that vanadyl pyrophosphate alone is the important VPO phase for selective oxidation of *n*-butane.

4.2. Organic catalysts

The organic synthesis route was more selective at producing vanadyl hydrogen phosphate hemihydrate than the aqueous route. Calcination of these precursors in nitrogen resulted in the formation of vanadyl pyrophosphate with no other crystalline phase detected by XRD. At higher P/V ratios during synthesis the crystalline order of the precursor was reduced, and this reduction in crystalline order carried through to the pyrophosphate catalyst. Raman spectroscopy identified orthophosphate phases in the catalysts calcined in oxygen.

The strong PO_4 Raman band at 921 cm^{-1} could mask the identity of the minor VPO phases, in which case the well-defined separation of paramagnetic and diamagnetic, i.e. chemical shift, ranges for VPO phases in ^{31}P NMR spectroscopy simplifies detection of even traces of amorphous $VOPO_4$ phases [16]. No diamagnetic $VOPO_4$ phases were identified by either XRD or Raman spectroscopy in the freshly calcined catalysts for P/V = 1.18 or 1.5. At high P/V ratios, formation of $VO(H_2PO_4)_2$ may be expected during synthesis, even in the organic medium, since water is produced during the reduction of V_2O_5. Formation of the dihydrogen phosphate can be determined by the presence of metaphosphates in the calcined samples. The peaks of $(VO)_2P_2O_7$ (ca. 2400 ppm) and $VO(PO_3)_2$ (ca. 750 ppm) are well separated, so the spin-echo spectrum of catalyst O:C:I:1.5 should give a clearer indication of the presence of $VO(PO_3)_2$. No metaphosphate was detected in the catalyst calcined at 823 K. However, in order to completely rule out the presence of $VO(PO_3)_2$, both the P/V = 1.18 and P/V = 1.5 catalysts were oxidized into diamagnetic V(V) orthophosphate phases. The linewidths in the ^{31}P MAS-NMR spectra of diamagnetic phases were considerably narrowed (FWHM of 6.5 ppm vs. ca. 1000 ppm in paramagnetic phases), allowing reliable detection of a number of $VOPO_4$ phases in the −25 to 10 ppm range [14,33]. V(V) dispersed in the matrix of paramagnetic $VO(PO_3)_2$ would appear in the diamagnetic range as an additional peak between −200 and −50 ppm (16b). The ^{31}P MAS-NMR spectrum of the orthophosphate phase at P/V = 1.18 did not show the presence of $VO(PO_3)_2$. Therefore, it was concluded that the organic catalysts did not contain $VO(PO_3)_2$ at the optimal synthetic P/V ratios in the 1.1–1.2 range. Traces of the metaphosphates were detected as a weak peak at −180 ppm at short relaxation delays (1–2 s) in the ^{31}P MAS-NMR spectrum. The bulk γ-$VOPO_4$ phase relaxed much slower and persisted for longer relaxation delay times (100 s). At the longer relaxation delay times only orthophosphate peaks were observed in the ^{31}P MAS-NMR spectrum. The content of the metaphosphate phases was estimated to be less than 2% based on integration of the area between −300 and −100 ppm and the peak of γ-$VOPO_4$ in this spectrum. This is in contrast to the aqueous derived catalysts where the metaphosphate phase was quite evident.

4.3. Model organic catalysts

The synthesis of model catalysts was designed to prepare vanadyl pyrophosphate catalysts with a platelet morphology which preferentially expose the (200) surfaces of vanadyl pyrophosphate. XRD identified only $VOHPO_4 \cdot 0.5H_2O$ in the catalyst precursor. Calcination of the vanadyl hydrogen hemihydrate precursors in nitrogen led to formation of vanadyl pyrophosphate, $(VO)_2P_2O_7$. Calcination of the catalysts in oxygen led to the appearance of a diffraction peak at 4.16 Å, which could not be accounted for by the (113) reflection of vanadyl pyrophosphate (observed at 4.07 Å). The (004) reflection in the powder XRD pattern of γ-$VOPO_4$ occurs

at 4.15 Å. The strongest reflection from the orthophosphate, the (221) reflection at 3.91 Å, coincides with the (020) reflection (3.88 Å) of vanadyl pyrophosphate. These results show that the calcination in oxygen results in partial oxidation of vanadyl pyrophosphate to form crystalline γ-$VOPO_4$.

XRD provides two parameters that are generally used to assess the size of crystallites and degree of structural (stacking fault) disorder of vanadyl pyrophosphate: the half-width of the (200) peak and the ratio of intensities of the (200) and (042) reflections [15]. The latter two reflections are related to respectively (001) and (130) reflections in the hemihydrate precursor [1]. The crystallinity of vanadyl pyrophosphate improved slightly with calcination in oxygen as seen in narrowing of the (200) reflection (Table 4).

Water washing of the calcined catalysts removed the γ-$VOPO_4$ as evidenced by the disappearance of the 4.16 Å peak in the XRD. However, the I_{200}/I_{042} ratio is dramatically increased (Table 4) and consistent with the reported value of 3 or 4.3 if based on integrated intensities [15]. The high ratios indicate both improved stacking of the platelet particles and the *bc* planes of vanadyl pyrophosphate within the individual platelets. However, the half-widths of the (200) reflection in the water washed pyrophosphate catalysts increased as compared to the calcined catalysts, in good agreement with the reported value of 0.78 [10]. The increase in FWHM of the (200) reflection indicates that the thickness of the platelet particles in the (100) direction decreased. The half-width of the (042) peak decreases slightly reflecting increased crystalline order of the *bc* planes as well. It should be noted that both the nitrogen calcined catalyst and the oxygen calcined water washed catalyst are single phase vanadyl pyrophosphates, but the water washed catalyst displays more structural order. This observation is important in comparing the performance of both catalysts in *n*-butane oxidation which is carried out below.

Traces of α-$VOHPO_4 \cdot 2H_2O$ were detected in the precursors of the organic catalysts by Raman spectroscopy, and the presence of some $VOPO_4$ phase was suggested by the displacement of the PO_4 of pyrophosphate from 921 cm^{-1} band to 924 cm^{-1}. Raman data revealed the dramatic impact of the calcination in oxygen on the phase composition of VPO system. In addition to vanadyl pyrophosphate a number of vanadyl(V) orthophosphates were detected in catalysts M:C:II:A and M:C:II:B. The water treatment suggested by Misono et al. [15] facilitated removal of some vanadium(V) orthophosphates that have finite solubility in water and form intensely colored solutions from orange–red to almost black depending on concentration. However, Raman data clearly demonstrated that the water washed catalyst still contained $VOPO_4$ phases which XRD method was incapable to detect.

The results of the kinetic studies performed on the model catalysts reported here indicate that much longer periods of time were necessary to achieve steady state operation than the 4 h reported by Misono et al. [15]. Our results indicate steady state performance only after 5–7 days under the reactive conditions and demonstrate that evolution of the active catalyst took nearly a week under reaction conditions. This was also found in an electron microscopy study, where crystalline ordering of the surface region of vanadyl pyrophosphate coincided with the reaction selectivity of *n*-butane to maleic anhydride [34]. The most selective catalyst contained no minor $VOPO_4$ phases. BET surface area measurements (Table 5) indicated that the as-synthesized catalyst had a low surface area of 9.0 m^2/g, which decreased further to 5.9 m^2/g after calcination in oxygen. After the soluble $VOPO_4$ phases were removed, the surface area increased dramatically to 31.5 m^2/g, which accounted for higher activity of the water washed catalyst in *n*-butane oxidation.

The experimental data obtained lend no support to the model of *n*-butane oxidation on micro crystalline domains of $VOPO_4$ phases

present in VPO catalysts [1,7]. The water treatment of catalysts resulted in removal of a considerable portion of the $VOPO_4$ phases with concurrent improvement of the reaction selectivity for maleic anhydride. The ^{31}P spin-echo NMR spectrum also showed the presence of only vanadyl pyrophosphate in the equilibrated catalyst. The results of the present work indicated that besides vanadyl(IV) pyrophosphate, no other phase either micro crystalline or amorphous was present in the best model catalysts. This work also showed that a clean vanadyl hydrogen phosphate hemihydrate precursor is critical to obtaining the most selective catalysts.

5. Conclusion

It has been shown that the coupling of analytic techniques, XRD, Raman spectroscopy and ^{31}P NMR spectroscopy can help identify amorphous and micro crystalline components of the VPO catalysts that influence their performance as catalysts. In most cases XRD was not effective at identifying the presence of these minor phases.

The results of the present work indicated that vanadyl pyrophosphate alone and no other minor VPO phase was responsible for selective oxidation of *n*-butane to maleic anhydride. The best model organic catalyst studied was pure vanadyl pyrophosphate by XRD and Raman and displayed the highest degree of stacking order. The presence of the inactive component, $VO(H_2PO_4)_2$, in the aqueous VPO precursors at high synthetic P/V ratios led to the suppression of the catalytic activity. This phase was not detected in the most selective organic catalysts at common synthetic P/V ratios (1.1–1.2). Microdomains of δ- and γ-vanadyl(V) orthophosphates in the model organic VPO catalysts were also found to be detrimental to their catalytic performance. The V(V) phases, which were detrimental to catalyst performance were shown to be removed by washing in boiling water, giving vanadyl pyrophosphate catalysts with the best selectivity for maleic anhydride.

The results presented here are in agreement with the model proposed by Centi [5] that vanadyl pyrophosphate serves as a support for an active surface layer. However, the detailed structure of this surface layer is still not understood.

Acknowledgements

This work was supported by the AMOCO Chemical Corporation and National Science Foundation Grant CTS-9100130. The authors wish to thank J. Forgac, M. Haddad and H. Taheri of Amoco Chemicals for their suggestions during the course of this work, and the assistance of Dr. G. Deo of Lehigh University with the Raman spectroscopy.

References

[1] E. Bordes, Catal. Today, 1 (1987) 499.
[2] P. Amorós, R. Ibáñez, E. Martínez-Tamayo, A. Beltrán-Porter, D. Beltrán-Porter and G. Villeneuve, Mater. Res. Bull., 24 (1989) 1347.
[3] G. Centi, F. Trifirò, J.R. Ebner and V.M. Franchetti, Chem. Rev., 88 (1988) 55.
[4] G. Centi, Catal. Today, 16 (1993) 5.
[5] Please see Catal. Today, 16 (1993) and references therein.
[6] (a) B.K. Hodnett, Catal. Rev., Sci. Eng., 27 (1985) 373; (b) G. Centi and F. Trifirò, Chim. Ind. (Milan), 68 (1986) 74; (c) B.K. Hodnett, Catal. Today, 1 (1987) 477; (d) P.A. Agaskar, L. DeCaul and R.K. Grasselli, Catal. Lett., 23 (1994) 339.
[7] (a) N. Harrouch Batis, H. Batis, A. Ghorbel, J.C. Vedrine and J.C. Volta, J. Catal., 128 (1991) 248; (b) M. Guilhoume, M. Roullet, G. Pajonk and J.C. Volta, in P. Ruiz and B. Delmon (Editors), New Developments in Selective Oxidation by Heterogeneous Catalysis, Elsevier, Amsterdam, 1992, p. 255; (c) J.C. Vedrine, J.M.M. Millet and J.C. Volta, Faraday Discuss. Chem. Soc. 87 (1989) 207.
[8] (a) H. Morishige, J. Tamaki, N. Miura and N. Yamazoe, Chem. Lett., (1990) 1513; (b) N. Yamazoe, H. Morishige, J. Tamaki and N. Miura, in L. Guczi et al. (Editors), New Frontiers in Catalysis, Elsevier, Amsterdam, 1993, p. 1979.
[9] H.E. Bergna, US Pat., 4,769,477, 1988; Assigned to E.I. Du Pont de Nemours and Co., Wilmington, DE.
[10] J.W. Johnson, D.C. Johnston, A.J. Jacobson and J.F. Brody, J. Am. Chem. Soc., 106 (1984) 8123.

[11] E. Bordes, P. Courtine and J.W. Johnson, J. Solid State Chem., 55 (1984) 270.
[12] I.E. Wachs and K. Segawa, in I.E. Wachs (Editor), Characterization of Catalytic Materials, Butterworth-Heinemann, Boston, 1992, p. 71.
[13] J.C. Volta, K. Bere, Y.J. Zhang and R. Olier, in S.T. Oyama and J.W. Hightower (Editors), Catalytic Selective Oxidation, ACS, Washington, DC, 1993, p. 217.
[14] F. Ben Abdelouahab, R. Olier, N. Guilhaume, F. Lefebvre and J.C. Volta, J. Catal., 134 (1992) 151.
[15] H. Igarashi, K. Tsuji, T. Okuhara and M. Misono, J. Phys. Chem., 97 (1993) 7065.
[16] (a) J. Li, M.E. Lashier, G.L. Schrader and B. Gerstein, Appl. Catal., 73 (1991) 83; (b) M.T. Sananes, A. Tuel and J.C. Volta, J. Catal., 145 (1994) 251.
[17] E. Bordes, P. Courtine and G. Pannetier, Ann. Chim. Paris, 8 (1973) 105.
[18] G. Villeneuve, A. Erragh, D. Beltrán, M. Drillon and P. Hagenmuller, Mater. Res. Bull., 21 (1986) 621.
[19] B.C. Tofield, G.R. Crane, G.A. Pasteur and R.C. Sherwood, J. Chem. Soc., Dalton Trans., (1975) 1086.
[20] A.V. Lavrov, L.S. Guzeeva and P.M. Fedorov, Izv. Akad. Nauk SSSR, Neorg. Mater., 10 (1974) 2180.
[21] T. Okuhara, K. Inumaru and M. Misono, in S.T. Oyama and J.W. Hightower (Editors), Catalytic Selective Oxidation, ACS, Washington, DC, 1993, p. 156.
[22] G. Ladwig, Z. Anorg. Allg. Chem., 338 (1965) 266.
[23] The circuit design provided by Dr. J. Schaefer and Mr. R. McKay of Washington University.
[24] M. Rance and R.A. Byrd, J. Magn. Reson., 52 (1983) 221.
[25] P. Weisz and D. Prater, Adv. Catal., 6 (1954) 143.
[26] A. Rulmont, R. Cahay, M. Liegeois-Duyckaerts and P. Tarte, Eur. J. Solid State Inorg. Chem., 28 (1991) 207.
[27] E. Bordes, J.W. Johnson, A. Raminosona and P. Courtine, Mater. Sci. Monogr., 28b (1985) 887.
[28] S.A. Linde, Yu.E. Gorbunova and A.V. Lavrov, Zh. Neorg. Khim., 28 (1983) 29.
[29] N. Middlemiss, F. Hawthorne and C. Calvo, Can. J. Chem., 55 (1977) 1673.
[30] P. Amorós, R. Ibáñez, A. Beltrán, D. Beltrán, A. Fuertes, P. Gomez-Romero, E. Hernandez and J. Rodriguez-Carvajal, Chem. Mater., 3 (1991) 407.
[31] A. Le Bail, G. Ferey, P. Amoros, D. Beltran-Porter and G. Villeneuve, J. Solid State Chem., 79 (1989) 169.
[32] Based on calibration mixtures of $VOHPO_4.0.5H_2O$ and $VO(H_2PO_4)_2$ of known composition.
[33] Unpublished ^{31}P NMR data: $VOPO_4 \cdot 2H_2O$ (8 ppm), γ-$VOPO_4$ (−18.7 ppm), δ-$VOPO_4$ (−16.4 ppm), β-$VOHPO_4$ (−11 ppm).
[34] V.V. Guliants, J.B. Benziger, S. Sundaresan, N. Yao and I.E. Wachs, Catal. Lett., 32 (1995) 379.